Microsc. Microanal. 3, 28–46, 1997

Microscopy AND Microanalysis

Theory of Lattice Resolution in High-angle Annular Dark-field Images

Adam Amali and Peter Rez*

Department of Physics and Astronomy and Center for Solid State Science, Arizona State University, Tempe, AZ 85287-1504

Abstract: The theoretical interpretation of lattice resolution in high-angle annular dark-field images produced in a scanning transmission electron microscope (STEM) has been a subject of controversy. A first-order perturbation theoretical analysis is presented here, which shows that the contrast in the image arises from large-angle multiphonon, incoherent scattering, which is atomic number dependent. The lattice resolution is a consequence of coherently filling the objective aperture, and dynamical elastic diffraction preceding the large-angle multiphonon scattering is not a necessary requirement. Elastic scattering to the higher order Laue zone (HOLZ) is also shown to be negligible, compared with the incoherent scattering. Calculations from application of the theory are also presented. They show that lattice images formed using the high-angle annular dark-field detector are sensitive to atomic number and are relatively insensitive to defocus. Although high-angle annular dark-field lattice imaging appears to be simple, scattering into the high-angle detector can only be approximately described by an incoherent imaging model.

Key words: high-angle annular dark-field, scanning transmission electron microscopy, lattice imaging

INTRODUCTION

In the scanning transmission electron microscope (STEM) a highly coherent source of energetic electrons is demagnified by means of lenses to form a nanoprobe that is rastered across the specimen. The probe electrons can be both elastically and inelastically scattered in their interaction with the specimen. The inelastically scattered electron distribution has a narrower angular distribution, and by judicious choice of collection apertures, an approximate separation can be made between the large-angle elastic scattering and the smaller-angle inelastic scattering. Furthermore, the inelastically scattered electrons can be energy analyzed by passing them through an energy loss spectrometer. Signals from all these detectors can be displayed on a monitor in synchronism with the raster of the probe, either individually or combined in an appropriate manner, to form scanned images.

Since the pioneering work of Crewe (Crewe, et al., 1968; Crewe and Wall, 1970) on the imaging of single heavy atoms by using the ratio of the annular detector signal and the small-angle bright-field signal, there has been considerable interest in the Z-contrast and related techniques as analytical tools for compositional and structural determination. Crewe argued that the annular dark-field signal would be proportional to the elastic scattering and the bright field would be proportional to the inelastic scattering. The ratio of elastic to inelastic scattering is approxi-

Received June 19, 1996; accepted September 5, 1996.

*Corresponding author

mately proportional to the atomic number, Z, according to the simple theory of Lenz. The annular aperture of Crewe et al. subtended a relatively small angle of 20 mrads and the signal in crystalline specimens was sensitive to diffraction effects. Howie (1979) suggested that an annular aperture with a large inner cutoff, such as 50 mrad at 100 kV, would only pick up high-angle Rutherford scattering that goes as Z^2, since the Bragg spots are attenuated by the Debye-Waller factor. His ideas have been very successfully applied in studies of heavy-metal catalyst particles on light-element support films. Treacy and Rice (1989) used the signal collected at high angle to estimate the number of atoms in a supported catalyst cluster. By making assumptions about particle shape, they used the digitized image to attempt a calibration of intensity increment per atom. They calculated that Pt clusters containing as few as three atoms on a 200-Å thick γ-alumina substrate would be detectable by using a probe of 3.5 Å. This has also lead to studies on appropriate scattering cross-sections for high-angle annular dark-field detectors (Pennycook et al., 1986).

Following the multislice calculations of Kirkland et al., who investigated the suitability of high-angle dark field to study the sites of surface adatoms, it was realized that lattice resolution of crystals was possible by using the high-angle annular dark-field (HAADF) signal (Kirkland et al., 1987; Loane et al., 1988). The first results were published by Pennycook and Boatner (1988) who applied the method to the high T_c superconductor $YBa_2Cu_3O_{7-\delta}$. Subsequently, Pennycook and Jesson used the technique to study Si and InP (Pennycook and Jesson, 1990) and Si/Ge multilayers (Pennycook and Jesson, 1991). These results were followed by HAADF lattice images from Si (110), Si (100), and InP (100) by Silcox and colleagues (Loane et al., 1991, 1992; Silcox et al., 1992; Hillyard and Silcox, 1993; Hillyard et al., 1993).

The theoretical interpretation of these images has been controversial. Pennycook and co-workers argued that, provided a probe smaller than interplanar spacing can be formed, the lattice will be resolved and the imaging can be understood on the basis of incoherent scattering. The theoretical description is then a simple sum of individual intensities from an assembly of incoherent scatterers. This idea was later modified (Pennycook and Jesson, 1990) to incorporate localization on atomic columns by the s-state Bloch waves that were selected by the convergent probe. From a practical perspective it then became possible to calculate the intensities in the image by convoluting a probe with a function representing the scattering of each column (Silcox et al., 1992; Hillyard et al., 1993). It was also shown that even for coherent elastic scattering, the scattering from each column was independent of scattering from other columns (Treacy and Gibson, 1993; Jesson and Pennycook, 1995). The independent scattering model was modified by considering scattering from multiphonon thermal diffuse processes instead of simple Rutherford scattering (Jesson and Pennycook, 1993, 1995). Under these circumstances there is no coherence in scattering between atomic columns, and the coherence in the beam direction only extends across a small number of atoms in the column (Jesson and Pennycook, 1995). Ideally, the contrast for each atomic column would be proportional to Z^2, independent of thickness. Calculations showing an atomic number–dependent saturation of column intensity with thickness suggest that this simple view should be modified by different absorption factors for the channeled states (Hillyard et al., 1993).

The other approach has involved the use of multislice calculations with periodic continuation to simulate the propagation of a probe through the solid. The amplitude scattered into a high-angle detector is summed for each slice of the calculation. Implicit in this approach is a belief that the probe is coherent and propagates through the crystal by coherent scattering processes. This view is consistent with the theory of Spence and Cowley (1978), who argued that lattice resolution in STEM comes about from coherently filling an objective aperture that subtends an angle greater than the relevant Bragg angle. Scattering into the high-angle detector either comes from single-phonon scattering (Wang and Cowley, 1989a,b) or as a result of averaging over many configurations of atomic displacements (Kirkland et al., 1987; Loane et al., 1991). The latter approach is equivalent to multiphonon scattering with an Einstein (constant frequency) dispersion relation for the phonons. It has also been suggested (Spence et al., 1989) that the image process is totally coherent and that the HAADF image arose solely from elastic scattering to the first-order Laue zone.

In the present work, we analyze scattering into the high-angle annular dark field detector by perturbation theory. The various mechanisms for large-angle scattering are examined and we show that in the high-angle limit multiphonon scattering, using an Einstein model for phonon dispersion is equivalent to Rutherford scattering. We show that single-phonon scattering is incorrect in both the small- and large-angle limits and that thermal diffuse scattering is more significant than elastic scattering to the first-order Laue zone. We also show that inelastic scattering could make a substantial contribution for light elements.

We then develop a general expression for HAADF imaging which incorporates the effects of the probe-forming lens, multiphonon large-angle scattering, and dynamical diffraction both before and after the large-angle scattering event. The effects of dynamical scattering after scattering into the HAADF detector can be neglected. Our theory shows that although the contrast can be understood on the basis of incoherent scattering, the lattice resolution is a coherent effect that arises from the interference among different wave-vector components of the probe that are separated by Bragg vectors, in accordance with the theory of Spence and Cowley (1978).

Finally, we present calculations showing the sensitivity to atomic number and the insensitivity to defocus or specimen thickness of HAADF lattice images. The resolution, as expected, depends on the size of the aperture and accelerating voltage. We also show that the effect can only approximately be described by the incoherent imaging theory, which implies a simple, local absorption-like potential.

High-angle Scattering

Contribution to HAADF Signal from Single Atom Scattering

The simplest description of high-angle scattering is Rutherford scattering, which assumes that the electrons interact independently with the coulomb potential from the atomic nuclei. The amplitude scattered by the wave vector, **s** or electron scattering factor, is

$$f_{el}(s) = \frac{2}{a_0}\frac{Z^2}{s^2} \tag{1}$$

where Z is the atomic number and a_0 the Bohr radius. The cross section is simply the square of the electron scattering factor. A problem with the Rurtherford cross section is that both the differential scattering cross section and the integrated scattering cross section become infinite as the scattering wave vector (or in the case of the integrated cross section the minimum scattering wave vector) tend to zero. This singularity can be removed by using a screened coulomb potential

$$V(r) = \frac{Ze^2}{4\pi\varepsilon_0 r}\exp(-\mu r) \tag{2}$$

where ε_0 is the permittivity of free space. The electron scattering factor becomes

$$f_{el}(s) = \frac{2Z}{a_0(s^2+\mu^2)} \tag{3}$$

and the cross section is well behaved as s tends to zero. The screening parameter, μ, is an attempt to incorporate the extra scattering due to the atomic electrons. This can be done exactly if the Mott formula for the electron scattering factor is used

$$f_{el}(s) = \frac{2}{a_0}\frac{[Z - f_X(s)]}{s^2} \tag{4}$$

where $f_X(s)$, the X-ray scattering factor, is the Fourier transform of the electron charge density and describes the coulomb scattering by the atomic electrons. The X-ray scattering factor $f_X(s)$ tends to Z as s tends to zero, which means that the electron scattering factor is well behaved in this limit and $Z - f_x(s)$ becomes $f'_X(s)s^2$. As s becomes large, $f_X(s)$ tends to zero and the electron scattering factor becomes identical to that for Rutherford scattering. A common parameterization for $f_X(s)$ is a sum of 4 Gaussians (Doyle and Turner, 1968)

$$\sum_j a_j \exp(-b_j s^2). \tag{5}$$

Care must be taken that Z in Equation 5 is made to equal to $\sum aj$, otherwise the electron scattering factor will describe scattering from ionized atoms.

Phonon Contribution to HAADF in Solids

So far we have considered scattering by isolated atoms. In a solid, elastic scattering is confined to the Bragg spots. Scattering between the Bragg spots only comes about from inelastic excitations. Plasmons and the majority of single-electron excitations only result in relatively small scattering angles of E/mv^2, where E is the energy loss and v is the electron velocity. Even at 100 kV this angle will not exceed 1 mrad for a 100 eV loss. Most of the scattering between Bragg spots comes from events involving the creation or destruction of acoustic phonons. Although the energy losses are small, usually less than 20 meV, the scattering angles can be quite large and are typically about 1 or 2 Bragg vectors (Rez et al., 1977). The theory for single-phonon scattering is

based on the expression for the structure factor in which the atom positions are shifted by displacements **u(r)** and can be found in standard solid-state physics textbooks (Kittel, 1986). In a simplified case, with one atom per unit cell, the phonon scattered amplitude $\phi(\mathbf{s})$ for scattering wave vector **s** is

$$\phi(\mathbf{s}) = f_{el}(s)(\exp[i\mathbf{s}.(\mathbf{r} + \mathbf{u}(\mathbf{r}))] - \exp[i\mathbf{s}.\mathbf{r}]) \tag{6}$$

For convenience, the scattering wave vector **s** is separated into a part inside the first Brillouin zone, **q**, and a reciprocal lattice vector **g**

$$\mathbf{s} = \mathbf{q} + \mathbf{g} \tag{7}$$

It is assumed that the displacements **u(r)** are small and that the product $\mathbf{s}.\mathbf{u}(\mathbf{r}) \ll 1$. This part of the exponential can then be expanded to first order to give the phonon scattering amplitude

$$\phi(\mathbf{s}) = i\mathbf{u} \cdot \mathbf{s} f_{el}(s)\exp(i\mathbf{s}.\mathbf{r}) \tag{8}$$

and hence the phonon scattering intensity is

$$dI(\mathbf{s}) = (\mathbf{u} \cdot \mathbf{s})^2 f_{el}^2(s)d\mathbf{s} \tag{9}$$

Assuming an isotropic phonon dispersion (relation between frequency and wave vector), averaging over angle, neglecting differences between transverse and longitudinal polarization and summing over processes involving both the creation and destruction of a phonon of wave vector **q** gives $\overline{u^2}$, the average displacement squared in terms of the occupation number N_q for phonons of wave vector **q**

$$\overline{u^2} = \frac{\hbar}{M_a\omega(q)}(N_q + 1/2) \tag{10}$$

The occupation number for a phonon of frequency ω, wave vector q, is given by the usual Bose-Einstein factor

$$N_q = \frac{1}{\left[\exp\left(\frac{\hbar\omega(q)}{k_BT}\right) - 1\right]} \tag{11}$$

where $\hbar$ is Plank's constant divided by 2π, k_B is Boltzmann's constant, and T is the temperature. Substituting equation 10 in equation 9 gives

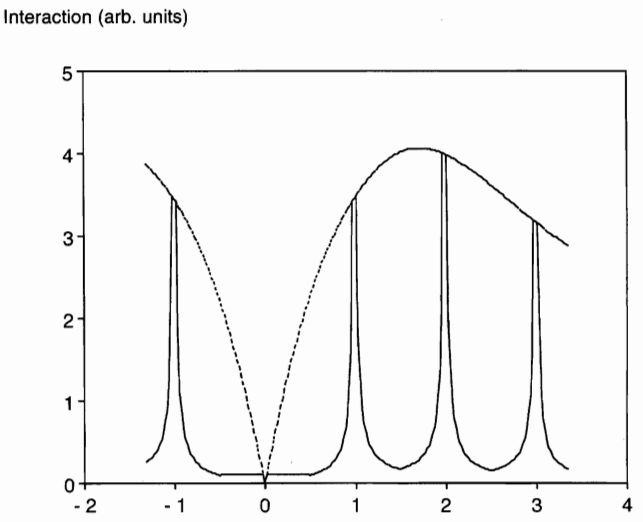

Figure 1. Intensity of phonon scattering for gold as a function of scattering wave vector showing the effects of the dispersion model. The scattering wave vector is in units of the 200 reciprocal lattice vector.

$$dI(\mathbf{s}) = \frac{\hbar}{M_a\omega(q)} s^2 f_{el}^2(s)\left(N_q + \frac{1}{2}\right)d\mathbf{s} \tag{12}$$

for the phonon scattered intensity.

For low-energy acoustic phonons at room temperature, $\hbar\omega(q) < k_BT$ and the Bose Einstein factor becomes

$$N_q \approx \frac{k_BT}{\hbar\omega(q)} \tag{13}$$

and the intensity is now

$$dI(\mathbf{s}) = \frac{\hbar k_BT}{M_a\omega^2(q)} s^2 f_{el}^2(s)d\mathbf{s} \tag{14}$$

This formula can be used to understand the distribution of single phonon scattering in diffraction patterns. The phonon frequency $\omega(q)$, like an energy band, is periodic from one Brillouin zone to the next. The overall intensity distribution is given by $s^2 f_{el}^2(s)$ which peaks approximately between the first and second reciprocal lattice point in a close packed direction for common metals and semiconductors (see Fig. 1). A simple treatment of the frequency of the phonon as a function of wave vector (the phonon dispersion relation), assuming the atoms can be treated as a linear chain in the wave-vector direction, gives

$$\omega(q) = \left(\frac{2C}{M_a}\right)^{\frac{1}{2}} \sin\left(\frac{1}{2}qa\right) \tag{15}$$

where C is the elastic constant and a is the repeat distance in the direction under consideration.

It can easily be seen that when q is small, the phonon dispersion is linear and can be approximated as $\omega(q) = v_s q$ where v_s is the speed of sound. This is called the *Debye model* for the dispersion relation and is of significance in the theory of the low temperature-specific heat. Examining equation 14 by using either equation 15, or the Debye dispersion, shows that the phonon scattered intensity will be peaked around the Bragg spots. Furthermore, the intensity for $\mathbf{s} = 0$ will tend to a constant value. A more sophisticated treatment of phonon dispersion (Begbie, 1947, Begbie and Born, 1947) where interactions of a three-dimensional lattice are considered leads to phonon dispersion relations in which low values of the frequency are found along simple crystallographic directions. According to equation 14, low frequencies mean higher intensities which appear as the thermal streaks often observed in diffraction patterns. It is not surprising that they are more easily observed around low-order reciprocal lattice points where the envelope term in equation 14 is peaked, though elastic dynamical diffraction will redistribute the intensity around all the reciprocal lattice points in the zero-order Laue Zone.

Another popular dispersion relation is the Einstein model in which it is assumed that the frequency is fixed at the Einstein frequency $\omega(q) = \omega_E$ and does not vary with the wave vector. This is actually quite a reasonable approximation for higher-frequency optic modes that are present when there is more than one atom per unit cell but, as can be seen from equation 15, it is totally inappropriate for the low-frequency acoustic modes that give rise to most of the scattering. Another way of looking at the Einstein model is to assume that atoms are independently vibrating at the Einstein frequency.

The phonon scattered intensity is now

$$dI(\mathbf{s}) = 4u^2 s^2 \frac{(Z - f_x(s))^2}{a_0^2 s^4} d\mathbf{s} \tag{16}$$

which behaves as

$$dI(\mathbf{s}) = \frac{4u^2 Z^2}{a_0^2 s^2} d\mathbf{s} \tag{17}$$

as s gets large and approaches zero as s tends to zero. Clearly this does not go to the same limits as Rutherford scattering either for small or large angles. A two-dimensional Fourier transform of the single-phonon scattering distribution (equation 16) will result in a doughnut-shaped function in real space, as seen in the calculations of Wang and Cowley (1989a,b). This effect has not been observed in the experimental images, which supports the idea that single-phonon scattering alone is not responsible for scattering to the HAADF detector.

For scattering angles greater than 50 mrad, **s.u** is greater than 0.5 and the simple first-order expansion of equation 6 is no longer valid (Konnert and D'Antonio, 1991). Higher-order terms in the expansion of the exponential in equation 6 have to be considered. Physically, these correspond to the creation or destruction of more than one phonon in the scattering event. The total scattering is derived from summing all such terms. This requires extensive computation if a realistic or even a Debye phonon dispersion is used, but it can be performed analytically if an Einstein dispersion relation is assumed (Earney, 1971). An approximate result for a general dispersion relation can be calculated by using the correlation function of Glauber (1955). This more sophisticated approach has been applied to HAADF imaging by Jesson (Jesson and Pennycook, 1995). Another way to derive the same result for the Einstein model is to follow the arguments of Hall and Hirsch (1965) which are given in Appendix A. The final expression for the multiphonon or thermal diffuse scattering cross section is equation A9

$$dI(\mathbf{s}) = 4\frac{(Z - f_x(s))^2}{a_0^2 s^4}[1 - \exp(-M\mathbf{s}^2)]ds \tag{18}$$

where M is the Debye-Waller factor, which can also be written in terms of the mean square atomic displacement if independently vibrating atoms are assumed. The Debye-Waller factor is given by

$$M = \frac{1}{2}\overline{u}^2 = \frac{\hbar}{2k_B M_a \theta_E}\left\{\frac{1}{\exp(\theta_E/T) - 1} + \frac{1}{2}\right\} \tag{19}$$

where θ_E is the Einstein temperature, which is related to the Einstein frequency by

$$\theta_E = \frac{\hbar\omega_E}{k_B} \tag{20}$$

Equation 18 tends to equation 1, the Rutherford scattering formula, as s becomes large, and approaches a constant value as s goes to zero. This behavior is to be expected as there should be no difference between atoms in a solid vibrating in an uncorrelated manner and free atoms in a dilute gas.

Although most inelastic scattering is confined to small angles, it is of interest to evaluate possible inelastic contributions to the HAADF detector. Scattering for valence and inner shell electrons involving large energy losses is concentrated as a momentum transfer equivalent to that for a free electron whose energy is identical to the energy loss of the fast electron. The resulting peak in the angular distribution of scattered intensity is known as the *Bethe ridge* (Egerton, 1986). A simple theory for the intensity is given in Appendix B. The approximate ratio of the elastically scattered intensity to the high-angle, inelastically scattered intensity is Z, the atomic number. For light elements such as carbon, this inelastic contribution could be significant and should be considered in quantitative imaging with the HAADF detector.

Elastic Scattering to Upper Layer Ring

Spence et al. (1989) have suggested that a substantial part of the signal collected by the HAADF detector comes from the first-order Laue zone ring. If this were true, the theory for the intensity collected would be quite different and there would be no doubt that the scattering and contrast arise from coherent diffraction effects. Pennycook showed experimentally that the contribution of the first-order Laue zone was about 1% of the thermal diffuse scattering intensity collected by the detector (Pennycook and Jesson, 1991). It is very easy to calculate the theoretical ratio of thermal diffuse to first-order Laue zone scattering, as both can be treated by first-order perturbation theory. The scattering for thermal diffuse scattering has been derived above and the integrated cross section for scattering to a detector with inner angle corresponding to wave vector $s_{\min}$ and outer angle corresponding to wave vector $s_{\max}$ is

$$\sigma = \int_{s_{\min}}^{s_{\max}} \frac{4(Z - f_x(s))^2}{K^2 a_0^2 s^4} [1 - \exp(-Ms^2)] 2\pi s ds \qquad (21)$$

where K is the fast electron wave vector. As the scattering is incoherent, the total scattering for an element with N atoms-unit volume of thickness t is $N\sigma t$.

The first order Laue zone (FOLZ) scattering is given by

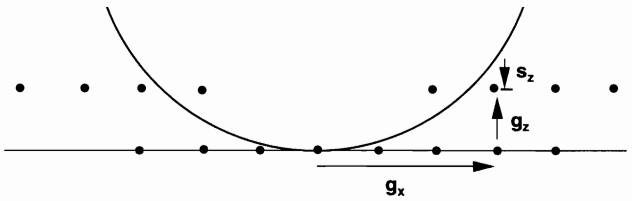

Figure 2. Geometry for scattering to the first order Laue zone (FOLZ).

the kinematic scattering expression, including the effects of the Debye Waller factor, which are significant for these high scattering angles. For example, in Si (110) at 100 kV, the FOLZ ring corresponds to an angle of 137 mrad. The cross section is

$$f_{el}^2(s) \frac{\sin^2(\pi t s_z)}{(\pi s_z)^2} \exp(-Ms^2) \qquad (22)$$

where the excitation error for upper layer line, s_z, is

$$s_z = \frac{1}{2\pi} \left[\frac{(g_x^2 + 2Kg_x\theta + 2K^2\theta^2)}{2K} - g_z \right] \qquad (23)$$

which is different from the normal expression used for the ZOLZ; as a correction, $2K^2\theta^2$ is added for the curvature of the Ewald sphere. A diagram showing the geometry is given as Figure 2. Even though the incident illumination spans a range of angles to form a disc in the diffraction pattern, only a limited set will contribute to the FOLZ due to the rapid attenuation by the term

$$\frac{\sin^2(\pi t s_z)}{(\pi s_z)^2} \qquad (24)$$

This is the reason why, in this simple theory, even with convergent beam illumination, the FOLZ appear as narrow lines whose width will be proportional to $1/s_z$. A more sophisticated treatment would consider "hybridization" with the Bloch waves from the ZOLZ, which will give further splittings (Buxton, 1976). One important point to note is the different thickness dependence of the FOLZ scattering, which varies as equation 24, and the thermal diffuse scattering, which is linear in thickness.

A calculation showing the intensities of FOLZ elastic scattering and thermal diffuse scattering for various thicknesses of Si (110) is given in Table 1. The FOLZ elastic

Table 1. Elastic HOLZ Scattering and Thermal Diffuse Scattering for Si (110).

Thickness	Thermal diffuse	HOLZ elastic
200 Å	1.29×10^{-4}	1.05×10^{-5}
400 Å	2.58×10^{-4}	2.28×10^{-5}
600 Å	3.87×10^{-4}	3.43×10^{-5}
800 Å	5.16×10^{-4}	4.23×10^{-5}
1000 Å	6.45×10^{-4}	5.66×10^{-5}

scattering is always less than 10%, which is probably still an overestimate because it assumes a value of 0.0045 $Å^{-2}$ for the mean square displacement at room temperature. Using this value to calculate a mean free path for attenuation by thermal diffuse scattering gives a value of 100 μ, which is probably too high by a factor of 10. The curvature of the Ewald sphere and the narrow width of the FOLZ line means that a multislice calculation must sample reciprocal space on a very fine grid with a spacing of about 0.1 mrad for a 500-Å crystal. This would mean a supercell about 200 Å across in a typical semiconductor or metal. Failure to sample at this high density could result in an overestimation of the elastic FOLZ intensity compared with the thermal diffuse intensity, since the calculation fails to select the very narrow regions of reciprocal space where elastic FOLZ scattering can occur. The results of multislice calculations on the ratio of elastic-to-thermal diffuse intensity should therefore be viewed with caution (Wang and Cowley, 1989a,b).

Imaging with Electrons Scattered to High Angles

Application to STEM Imaging

The theory for STEM imaging has been discussed extensively by Cowley (1973a,b) and by Spence and Cowley (1978). The ideas come from the reciprocal relationship between STEM and high-resolution TEM. In STEM, the field emission source is equivalent to a point in the detector plane in TEM if the objective aperture is coherently filled. Points in the detector in the STEM then become equivalent to different positions in the TEM source. The amplitude observed in the detector plane in the STEM is given by

$$\phi(\mathbf{s},\mathbf{r}_p) = \int H(\mathbf{s}-\mathbf{k})\Psi(\mathbf{k})\exp[-i\mathbf{k}\cdot\mathbf{r}_p]d^2\mathbf{k} \qquad (25)$$

where $H(\mathbf{s}-\mathbf{k})$ represents the scattering of a thin object, $\Psi(\mathbf{k})$ the effects of the object lens, $\mathbf{r}_p$ is the probe position, $\mathbf{k}$ is a wave vector of the incident probe forming electrons, and $\mathbf{s}$ is a wave vector for the scattered electron. The function $\Psi(\mathbf{k})$ representing the objective lens can now be expressed in terms of the aperture function $A(\mathbf{k})$, which is 1 inside the aperture and 0 elsewhere, and the wave-front aberration function $\kappa(\mathbf{k})$.

$$\Psi(\mathbf{k}) = A(\mathbf{k})\exp[i\chi(\mathbf{k})] \qquad (26)$$

$$\chi(k) = \pi\lambda\left(\Delta f\cdot k^2 + \frac{1}{2}C_s\lambda^2k^4\right) \qquad (27)$$

The intensity, of course, is the square of the amplitude at the detector plane

$$I(\mathbf{s},\mathbf{r}_p) = |\phi(\mathbf{s},\mathbf{r}_p)|^2 \qquad (28)$$

To explicitly bring out the variation of the signal with probe position, it is best to decompose the incident wave vector as $\mathbf{k} = \mathbf{q} + \mathbf{g}$, where $\mathbf{q}$ is a wave vector in the first Brillouin zone and $\mathbf{g}$, $\mathbf{h}$ are reciprocal lattice vectors in the zero-order Laue zone. The intensity for a slice dz becomes

$$dI(\mathbf{s},\mathbf{r}_p) = \int\sum_{gh} H(\mathbf{s}-\mathbf{q}-\mathbf{g})H^*(\mathbf{s}-\mathbf{q}-\mathbf{h}) A(\mathbf{q}+\mathbf{g})A(\mathbf{q}+\mathbf{H})\times\exp[i\chi(\mathbf{q}+\mathbf{g})] \exp[-i\chi(\mathbf{q}+\mathbf{h})]\exp[-i(\mathbf{g}-\mathbf{h})\cdot\mathbf{r}_p]d^2\mathbf{q}dz \qquad (29)$$

where the integral over $\mathbf{q}$ representing different phonon wave vectors is over the first Brillouin zone. If it is assumed that atoms vibrate independently according to an Einstein model then it is obvious that scattering from different slices should be added incoherently. Even when phonon modes are explicitly considered, the range of coherence is no more than a few atomic layers (Jesson and Pennycook, 1995; see also Appendix A). The probe is defined by the aperture functions $A(\mathbf{q}+\mathbf{g})$ and the wave-front aberration function $\chi(\mathbf{q}+\mathbf{g})$. Equation 29 is a Fourier series with an expansion in terms of lattice vectors. There can only be Fourier coefficients if the incident range of wave vectors, as defined by the illumination aperture, is greater than the size of the Brillouin zone, as shown in Figure 3. This is precisely the point made by Spence and Cowley (1978), who showed that lattice resolution is possible only if the probe objective aperture semi-angle is greater than half a Bragg angle. From

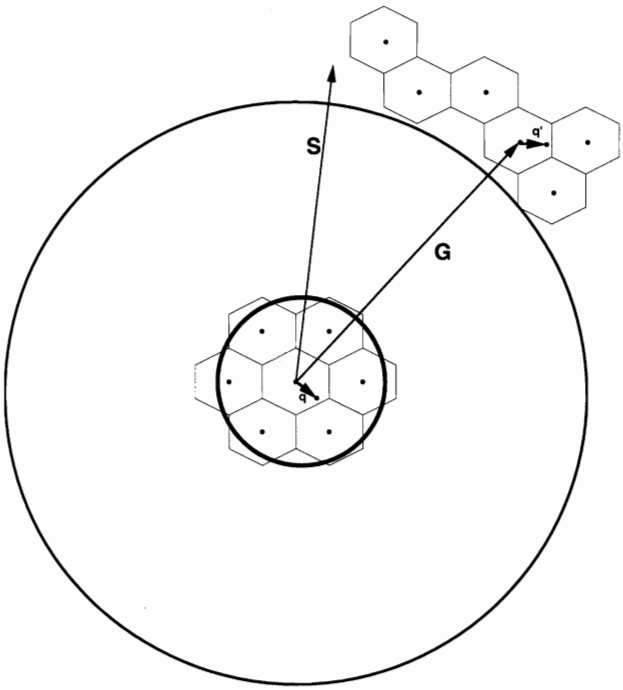

Figure 3. Diagram showing scattering in reciprocal space.

the uncertainty principle this is equivalent to saying that the probe size is less than the relevant lattice plane spacing if the probe is coherent. The magnitude of the Fourier coefficients is determined both by the electron optical parameters found in the wave-front aberration function and the scattering in the specimen. The theory for multiphonon scattering in the specimen has been given in Appendix A. The HAADF signal can be obtained by integrating equation 29 over the specimen thickness and the annular aperture and using equation A11 from the appendix for the product of multiphonon scattering matrix elements.

$$I(\mathbf{r}_p) = t\int\int\sum_{gh} H(\mathbf{s}-\mathbf{q}-\mathbf{g})H^*(\mathbf{s}-\mathbf{q}-\mathbf{h})A(\mathbf{q}+\mathbf{g})$$
$$A(\mathbf{q}+\mathbf{h})\times\exp[i\chi(\mathbf{q}+\mathbf{g})]\exp[-i\chi(\mathbf{q}+\mathbf{h})]$$
$$\exp[-i(\mathbf{g}-\mathbf{h})\cdot\mathbf{r}_p]d^2\mathbf{q}d^2\mathbf{s} \qquad (30a)$$

$$H(\mathbf{s}-\mathbf{q}-\mathbf{g})H^*(\mathbf{s}-\mathbf{q}-\mathbf{h}) =$$

$$\frac{4}{K^2a_0^2V_c}\sum_i \exp(-i(\mathbf{g}-\mathbf{h})\cdot\mathbf{r}_i)$$
$$\frac{[Z_i-f_x^i(s-q-g)][Z_i-f_x^i(s-q-h)]}{(\mathbf{s}-\mathbf{q}-\mathbf{g})^2(\mathbf{s}-\mathbf{q}-\mathbf{h})^2}$$
$$\times\{\exp[-M_i(\mathbf{g}-\mathbf{h})^2]-\exp[-M_i(\mathbf{s}-\mathbf{q}-\mathbf{g})^2]$$
$$\exp[-M_i(\mathbf{s}-\mathbf{q}-\mathbf{h})^2]\} \qquad (30b)$$

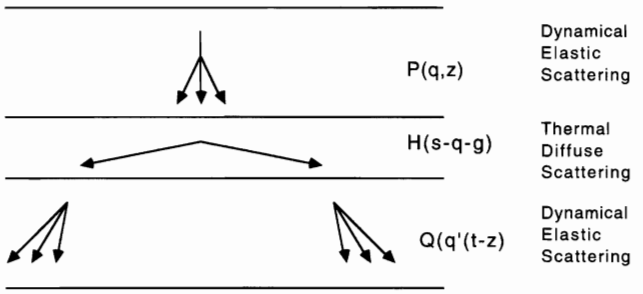

Figure 4. Schematic figure for thermal diffuse scattering in a crystal.

It is important to note that so far, we have not included elastic scattering, and that it is not necessary for elastic scattering to take place to achieve lattice resolution in high-angle annular dark-field STEM.

Elastic Scattering before or after Large-angle Multiphonon Scattering

So far we have only considered thermal diffuse scattering to large angles. In the electron microscopy of crystalline specimens there is always strong elastic scattering, especially among beams in the zero-order Laue zone. It is therefore necessary to consider multiple elastic scattering (dynamical diffraction) both before and after the large-angle thermal diffuse scattering event. This is shown schematically in Figure 4. The simplest way to represent dynamical diffraction is to use matrix operators that represent the redistribution of complex amplitude among a set of Bragg beams. They can be formally derived from the Greens functions solutions for the elastic scattering interactions (Dudarev et al., 1993). These matrices are functions of crystal orientation, which is best represented by a wave vector in the first Brillouin zone. Let $Q_{GH}(\mathbf{q}',t-z)$ be the matrix that represents redistribution among Bragg beams defined by wave vector $\mathbf{q}'$ and $P_{gh}(\mathbf{q},z)$ be the matrix that represents redistribution among beams for incident radiation defined by wave vector $\mathbf{q}$. The matrices can be calculated by any of the methods used in the theory of dynamical diffraction, such as the direct integration of the Howie-Whelan equations (Hirsch et al., 1965), multislice calculations (Goodman and Moodie, 1974), expressions involving tight-binding Bloch waves (Buxton et al., 1978), or Bloch waves expressed as sums of plane waves. For convenience, we shall use Bloch waves that are the sums of plane wave, in which case $Q_{GH}(\mathbf{q}',t-z)$ and $P_{gh}(\mathbf{q},z)$ become

$$P_{gh}(\mathbf{q},z) = \sum_i C_g^i(\mathbf{q})C_h^i(\mathbf{q})\exp[ik_z^i(\mathbf{q})z] \tag{31}$$

$$Q_{GL}(\mathbf{q}',t-z) = \sum_{j'} D_G^{j'}(\mathbf{q}')D_L^{j'}(\mathbf{q}')\exp[ik_z^{j'}(\mathbf{q}')(t-z)] \tag{32}$$

The scattering amplitude to the HAADF detector can then be represented in Fourier space by the function describing the probe, the dynamical elastic scattering in the specimen (equation 31), the thermal diffuse scattering to high angle, $H(\mathbf{q}' + \mathbf{L} - \mathbf{q} - \mathbf{g})$, and any subsequent dynamical diffraction of the electrons scattered to high angles (equation 32). The wave vector of the electrons scattered into the HAADF detector is given by $\mathbf{q}' + \mathbf{L}$ where $\mathbf{q}'$ is in the first Brillouin zone and $\mathbf{L}$ is an appropriate reciprocal lattice vector for the HAADF detector (see Fig. 3). The scattering amplitude is

$$\begin{aligned} d\phi(\mathbf{r}_p,\mathbf{q}' + \mathbf{L}) = {} & Q_{GL}(\mathbf{q}',t-z)H(\mathbf{q}' + \mathbf{L} - \mathbf{q} - \mathbf{g})P_{gh}(\mathbf{q},z) \\ & A(\mathbf{q} + \mathbf{h})\exp[i\chi(\mathbf{q} + \mathbf{h})]\exp(i(\mathbf{q} + \mathbf{h}) \cdot \mathbf{r}_p)dz \end{aligned} \tag{33}$$

The intensity in the dark field detector is given by

$$\begin{aligned} dI(\mathbf{r}_p,\mathbf{q}' + \mathbf{G}) = {} & \sum_{\substack{L,L' \\ g,g',h,h'}} \iiint Q_{GL}(\mathbf{q}',t-z)Q^*_{G'L'}(\mathbf{q}', t-z) \\ & H(\mathbf{q}' + \mathbf{L} - \mathbf{q} - \mathbf{g})H^*(\mathbf{q}' + \mathbf{L}' - \mathbf{q} - \mathbf{g}') \\ & \times P_{gh}(\mathbf{q},z)P^*_{g'h'}(\mathbf{q},z)A(\mathbf{q} + \mathbf{h})A(\mathbf{q} + \mathbf{h}') \\ & \times \exp[i_X(\mathbf{q} + \mathbf{h})]\exp[-i_X(\mathbf{q} + \mathbf{h}')] \\ & \exp[-i(\mathbf{h} - \mathbf{h}') \cdot \mathbf{r}_p]d^2\mathbf{q}dz \end{aligned} \tag{34}$$

It should be noted that the products of the dynamical diffraction propagator matrices are in fact elements of the density matrix, which has been used previously in the theory of high-energy electron scattering by Dudarev and Ryazonov (1988), Rez (1977), and Wright and Bird (1992). The Bloch wave expressions (equations 31 and 32) for the propagation matrices could be substituted in equation 35 and the integration over z performed explicitly to give

$$\begin{aligned} \mathrm{I}(\mathbf{r}_p) = {} & \sum_{\substack{G,G',L,L' \\ g,g',h,h'}} \iint D_G^{j'}D^{*i'}_G D^{*j'}_L D_L^{i'} C_g^i C^{*i}_h C^{*j}_g C_{h'}^j, \\ & \times \frac{\exp[i(k^i - k^j)t] - \exp[i(k^{j'} - k^{i'})t]}{(k^i - k^j - k^{i'} - k^{j'})} H(\mathbf{q}' + \mathbf{L} - \mathbf{q} - \mathbf{g}) \\ & H^*(\mathbf{q}' + \mathbf{L}' - \mathbf{q} - \mathbf{g}') \times A(\mathbf{q} + \mathbf{h}')A(\mathbf{q} + \mathbf{h}') \\ & \exp[i_X(\mathbf{q} + \mathbf{h})]\exp[-i_X(\mathbf{q} + \mathbf{h}')] \\ & \exp[-i(\mathbf{h} - \mathbf{h}') \cdot \mathbf{r}_p]d^2\mathbf{q}d^2\mathbf{q}' \end{aligned} \tag{35}$$

where the dependence on $\mathbf{q}$ or $\mathbf{q}'$ in the Bloch wave excitation coefficients and the wave vector k^i have been dropped for simplicity.

At this time we should note that the Bloch wave expansion for the scattered wave is made up from plane wave components with reciprocal lattice vectors in the first-order Laue zone. This is because only plane waves with excitation errors close to the Ewald sphere are excited, as shown in Figure 2. The mathematical consequence is that these Bloch waves from a complete set of states and the expressions given in equations 34 and 35 can be considerably simplified due to the orthonormality relations. The final state Bloch wave coefficients satisfy

$$\sum_G D_G^{j'}(\mathbf{q})D_G^{i'}(\mathbf{q}) = \delta_{i'j'}$$

$$\sum_{i'} D_L^{i'}(\mathbf{q})D_L^{i'}(\mathbf{q}) = \delta_{LL'} \tag{36}$$

and equation 35 reduces to

$$\begin{aligned} I(\mathbf{r}_p) = {} & \sum_{\substack{L,L',G,G' \\ g,g',h,h'}} \iint C_g^i C^{*i}_h C^{*j}_{g'} C_{h'}^j \frac{\exp[i(k^i - k^j)t] - 1}{(k^i - k^j)} \\ & H(\mathbf{q}' + \mathbf{L} - \mathbf{q} - \mathbf{g})H(\mathbf{q}' + \mathbf{L} - \mathbf{q} - \mathbf{g}') \times A(\mathbf{q} + \mathbf{h}) \\ & A(\mathbf{q} + \mathbf{h}')\exp[i_X(\mathbf{q} + \mathbf{h})]\exp[-i_X(\mathbf{q} + \mathbf{h}')] \\ & \exp[-i(\mathbf{h} - \mathbf{h}') \cdot \mathbf{r}_p]d^2\mathbf{q}d^2\mathbf{q}' \end{aligned} \tag{37}$$

Physically this means that it is not necessary to be concerned about redistribution among the Bragg beams if an integration over all final state beams is performed. The sum over scattered state reciprocal lattice vector can now be replaced by an integral over the annular dark-field detector.

$$\begin{aligned} I(\mathbf{r}_p) = {} & \int\int \sum_{\substack{ADF \\ g,g' \\ h,h'}} \iint C_g^i C^{*i}_h C^{*j}_g C_{h'} \frac{\exp[i(k^i - k^j)t] - 1}{(k^i - k^j)} \\ & H(\mathbf{s} - \mathbf{q} - \mathbf{g})H(\mathbf{s} - \mathbf{q} - \mathbf{g}') \times A(\mathbf{q} + \mathbf{h}) \\ & A(\mathbf{q} + \mathbf{h}')\exp[i_X(\mathbf{q} + \mathbf{h})]\exp[-i_X(\mathbf{q} + \mathbf{h}')] \\ & \exp[-i(\mathbf{h} - \mathbf{h}') \cdot \mathbf{r}_p]d^2\mathbf{q}d^2\mathbf{s} \end{aligned} \tag{38}$$

where the product $H(\mathbf{s} - \mathbf{q} - \mathbf{g})H(\mathbf{s} - \mathbf{q} - \mathbf{g}')$ is given by the expression A11 of Appendix A for thermal diffuse scattering, which was also used in equation 30. There is no requirement to use the Bloch wave formalism to calculate the effects of dynamical diffraction. One could explicitly leave

the expression in terms of the matrix propagator, which could then be evaluated by other methods such as multislice

$$I(\mathbf{r}_p) = \int\int_{ADF} \sum_{\substack{g,g' \\ h,h'}} \int\int H(\mathbf{s}-\mathbf{q}-\mathbf{g})H(\mathbf{s}-\mathbf{q}-\mathbf{g}') P_{gh}(\mathbf{q},z)P^*_{g'h'}(\mathbf{q},z) \times A(\mathbf{q}+\mathbf{h})A(\mathbf{q}+\mathbf{h}')\exp[i\chi(\mathbf{q}+\mathbf{h})] \exp[-i\chi(\mathbf{q}+\mathbf{h}')]\exp[-i(\mathbf{h}-\mathbf{h}')\cdot\mathbf{r}_p]d^2\mathbf{q}d^2\mathbf{s} \quad (39)$$

In a multislice calculation it is more efficient to calculate the matrices $P_{gh}(\mathbf{q},z)$ for all $\mathbf{q}$ values at the same time. This could be done by performing the calculation by using a supercell whose size is determined by how precisely one needs to sample in the Brillouin zone. For example, if a sampling of 8 points along the [200] direction is considered adequate, then a cell 16 times the [100] direction would be needed. The probe could then be represented as the Fourier transform of equation 26 localized at a particular position in the supercell. The advantage of working with the Bloch wave formalism (or any other formalism that retains the reciprocal lattice summations of equations 38 and 39) is that the Fourier coefficients of the image intensity, which were used by Hillyard and Silcox (1993) and by Loane et al. (1992) to characterize experimental images, are calculated explicitly.

As can be seen by comparing equations 30 with 38 and 39, the only effect of dynamical elastic diffraction is to interpose the matrix product $P_{gh}(\mathbf{q},z)P^*_{g'h'}(\mathbf{q},z)$ between the coherent electron probe and the thermal diffuse scattering. This might lead to changes in the magnitudes of the Fourier coefficients of the HAADF image and alter the contrast of the lattice fringes. The formalism incorporating elastic scattering before the thermal-diffuse, large-angle scattering is essential for explaining the contrast of defects such as dislocations, which were observed in the HAADF detector by Cowley and Huang (1992) and Perovic et al. (1993). Such contrast might require more than one Bloch wave, as an oscillating contrast is conventionally explained in terms of interbranch transitions (Hirsch et al., 1965). This is inconsistent with the expression given by Pennycook and Jesson (1990), where only one *s*-state Bloch wave is considered.

Equations 30 and 39, representing both the case of thermal diffuse scattering on its own and thermal diffuse scattering preceded by elastic scattering, can both be expressed in terms of a function $F(\mathbf{q},\mathbf{h},\mathbf{h}')$ which describes the scattering to the HAADF detector by the specimen and those terms which represent the incident probe.

$$I(\mathbf{r}_p) = \sum_{h,h'} \int\int F(\mathbf{q},\mathbf{h},\mathbf{h}')A(\mathbf{q}+\mathbf{h})A(\mathbf{q}+\mathbf{h}') \exp[i\chi(\mathbf{q}+\mathbf{h})]\exp[-i\chi(\mathbf{q}+\mathbf{h}']\exp[-i-\mathbf{h}')\cdot\mathbf{r}_p]d^2\mathbf{q} \quad (40)$$

where

$$F(\mathbf{q},\mathbf{h},\mathbf{h}') = \frac{1}{V_c}\int_0^t\int\int_{ADF} H(\mathbf{s}-\mathbf{q}-\mathbf{g})H(\mathbf{s}-\mathbf{q}-\mathbf{g}') P_{gh}(\mathbf{q},z)P^*_{g'h'}(\mathbf{q},z)d^2\mathbf{s}dz \quad (41)$$

when dynamical elastic scattering precedes thermal diffuse scattering into the HAADF detector and

$$F(\mathbf{q},\mathbf{h},\mathbf{h}') = \frac{1}{V_c}\int\int_{ADF} H(\mathbf{s}-\mathbf{q}-\mathbf{h})H(\mathbf{s}-\mathbf{q}-\mathbf{h}')d^2\mathbf{s} \quad (42)$$

when there is only thermal diffuse scattering. It would be particularly convenient if the part describing the effects of scattering in the specimen could be represented by a local scattering function and the HAADF intensity given by the incoherent imaging expression

$$I(r) = F(r)|\psi(r)|2 \quad (43)$$

Taking the Fourier transform, it can be seen that the scattering in the specimen, $F(\mathbf{q},\mathbf{h},\mathbf{h}')$, must be functions of $\mathbf{h} - \mathbf{h}'$

$$F(\mathbf{q},\mathbf{h},\mathbf{h}') = F(\mathbf{q},\mathbf{h} - \mathbf{h}') \quad (44)$$

As can be seen by examining equation 30b, this is only true in the limit where **s,** the scattering vector to the high-angle detector, is much greater than **g** and **h,** the reciprocal lattice vectors in the zero-order Laue zone. The scattering vectors $\mathbf{s} - \mathbf{q} - \mathbf{g}$ and $\mathbf{s} - \mathbf{q} - \mathbf{h}$ are then approximately equal to **s** and equation 30b becomes

$$H(\mathbf{s}-\mathbf{q}-\mathbf{g})H^*(\mathbf{s}-\mathbf{q}-\mathbf{h}) \approx \frac{4}{a_0^2 V_c}\sum_i \exp(-i(\mathbf{g}-\mathbf{h})\cdot\mathbf{r}_i) \frac{Z_i^2}{s^4}\exp[-M_i(\mathbf{g}-\mathbf{h})^2] \quad (45)$$

The error in making this assumption can be estimated by expanding equation 30b to first and second order in **g** and **h.** The fractional error, Δf, ignoring **q** compared with ***s*** is

$$\Delta f \approx 2\left[\frac{s^2}{f_x(s)}\frac{df_x(s)}{d(s^2)} - 1 - Ms^2\right]\frac{s\cdot(\mathbf{g}+\mathbf{h})}{s^2} + 2\left[\frac{s^4}{f_x(s)}\frac{d^2f_x(s)}{d(s^2)^2} + 2 + M^2s^4\right]\frac{(\mathbf{s}\cdot\mathbf{g})^2+(\mathbf{s}\cdot\mathbf{h})^2}{s^4} + \left[\frac{s^2}{f_x(s)}\frac{df_x(s)}{d(s^2)} - 1 - Ms^2\right]\frac{g^2+h^2}{s^2}. \quad (46)$$

The first two terms involving $\mathbf{s}\cdot\mathbf{g}$ and $\mathbf{s}\cdot\mathbf{h}$ average to zero for an annular detector, leaving the third (second-order) term, which is of order 5%, assuming that a zero-order Laue zone reciprocal lattice vector corresponds to about 10 mrad and the detector corresponds to about 100 mrad.

To summarize, the lattice resolution is a consequence of the incident semi-angle being greater than half the Bragg angle for the relevant lattice planes, while the contrast depends on the Fourier coefficients of the scattering as given in equations 38 and 39. These depend on the magnitude of the thermal diffuse (multiphonon) scattering, the elastic scattering in the crystal, and the electron optical parameters that determine probe size. Only calculation can determine the relative importance of all these effects, which will be explored in the next section.

Calculations

A program was written based on equation 38 in which the dynamical elastic diffraction is based on a Bloch wave representation. The program is structured as a number of nested loops. The outermost loops integrate over the Brillouin zone. At each point, the Bloch wave coefficients and wave vectors are determined by diagonalisation of the complex Hamiltonian matrix. The summations over the reciprocal lattice indices *g,g',h,h'* were then performed and the integration over the ADF detector, which only affected thermal diffuse scattering matrix elements (equation A11), was left as the innermost loop. The calculation time is dominated by the quadruple sum over *g,g',h,h'* and therefore scales as the fourth power of the number of ZOLZ reciprocal lattice vectors. For Si we used 13 vectors, which resulted in computation times of 11 minutes on a SGI IRIS workstation, and for InP we used 19 vectors, which increased the computation time to about 1 hour. The ADF detector was split into 5 radial and 10 angular segments for this integration. In all cases except where otherwise stated, the ADF detector accepted electrons scattered between 70 mrads and 200 mrads. A multislice calculation would scale as the squre of the numbers of ZOLZ lattice vectors multiplied by the number of thicknesses and the number of probe positions.

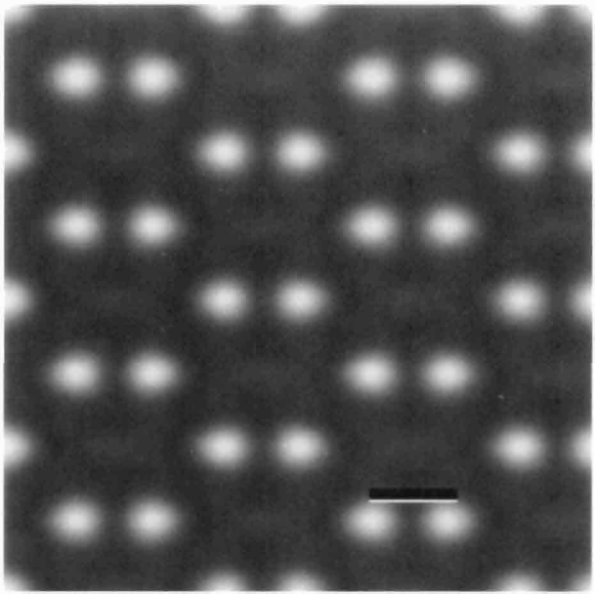

Figure 5. Si[110] HAADF simulated image for 1000-Å specimen from thermal diffuse scattering only (Equation 30) for 16.5 mrad objective aperture, C_s 0.8 mm, defocus 800 Å, accelerating voltage 100 kV. Bar: 1.36 Å.

We have used the program to calculate HAADF images and line profiles for the [110] and [100] projections of Si, GaAs, and InP, as these have been extensively studied experimentally. Figure 5 shows a calculation for 1,000 Å of Si in the [110] projection for 100kV electrons where only the thermal diffuse scattering as given by equation 30 is considered. The objective aperture of 16.5 mrad is more than sufficient to accommodate the 400 reciprocal lattice vector and the dumbbells are clearly resolved. This image also shows that dynamical diffraction before thermal diffuse scattering is not a necessary condition for lattice resolution.

The effects of the objective aperture size can be seen in Figure 6, which shows calculated images using 13 beams for 1000 Å of Si in the [110] projection at 100 kV. The line profiles along the [100] direction in the 800 Å defocus

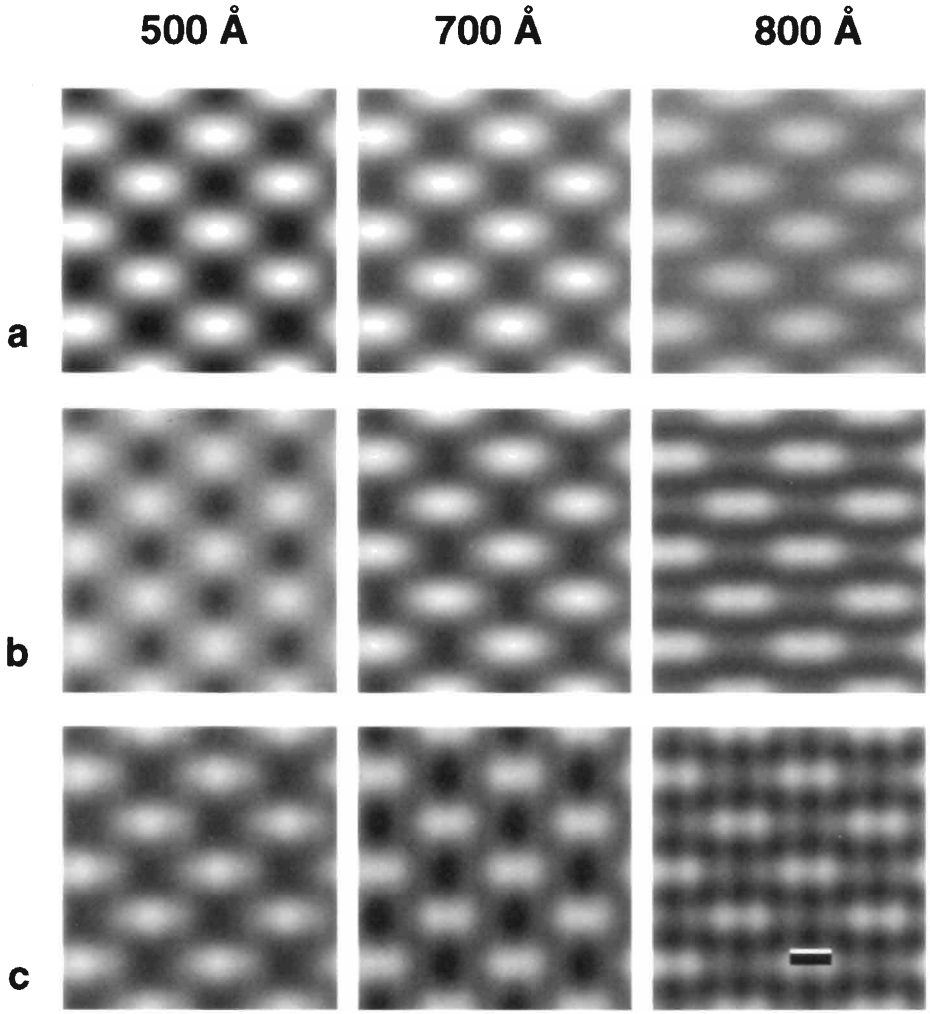

Figure 6. Si[110] HAADF simulated images for 1000-Å specimen, C_s 0.8 mm, accelerating voltage 100 kV for objective apertures of (**a**) 10.6 mrad, (**b**) 13.7 mrad, and (**c**) 16.5 mrad. Bar: 1.36 Å.

images are shown as Figure 7. From the line profiles, the use of a 10.3-mrad aperture, which only includes the 111 and 220 reciprocal lattice vectors, does not resolve the dumbbells. When the aperture semi-angle is increased to 13.7 mrad, the two peaks are barely apparent but are clearly resolved with a 16.5 mrad aperture, which includes reciprocal lattice vectors up to 400. Otherwise, the images are relatively insensitive to defocus. Increasing the accelerating voltage to 300 kV will of course result in a smaller probe size and improved resolution. Images for apertures of 7.5 mrad semi-angle, which is approximately equivalent to a 400 reciprocal lattice vector, 12.0 mrad and 19.5 mrad, are shown for defocus values of 400 Å and 600 Å in Figure 8. In all cases the dumbbells are clearly resolved.

One of the strongest arguments for using HAADF imaging is that the signal should show strong dependence on atomic number, which would make it possible to easily

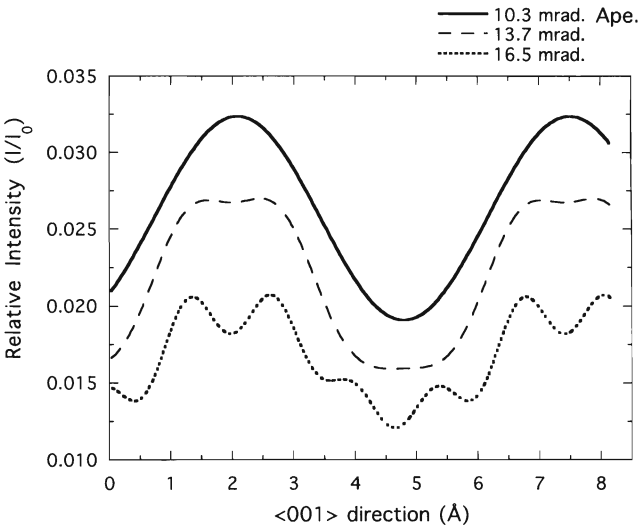

Figure 7. Line profiles along the [001] direction from the 800 Å defocus images of Figure 6.

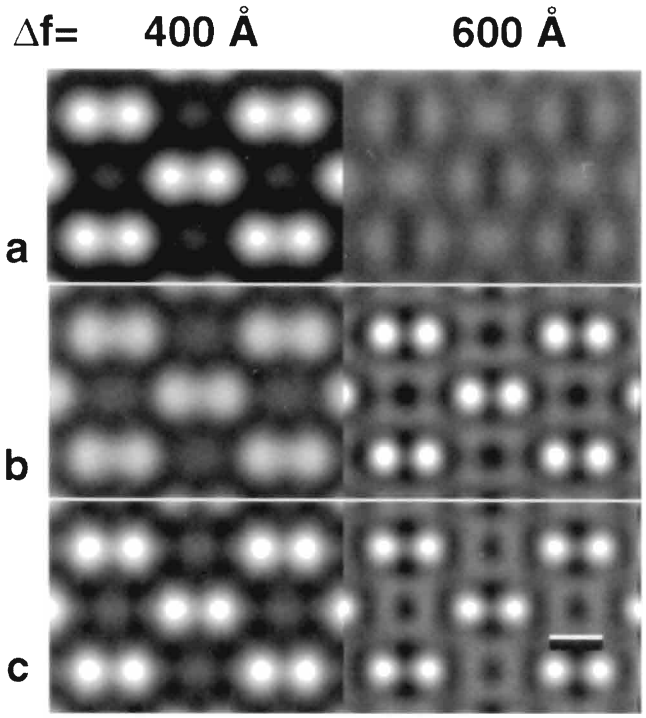

Figure 8. Si [110] HAADF simulated images for 1000-Å specimen, C_s 0.8 mm, accelerating voltage 300 kV for objective apertures of (**a**) 7.5 mrad (**b**) 12.0 mrad, and (**c**) 19.5 mrad. Bar: 1.36 Å.

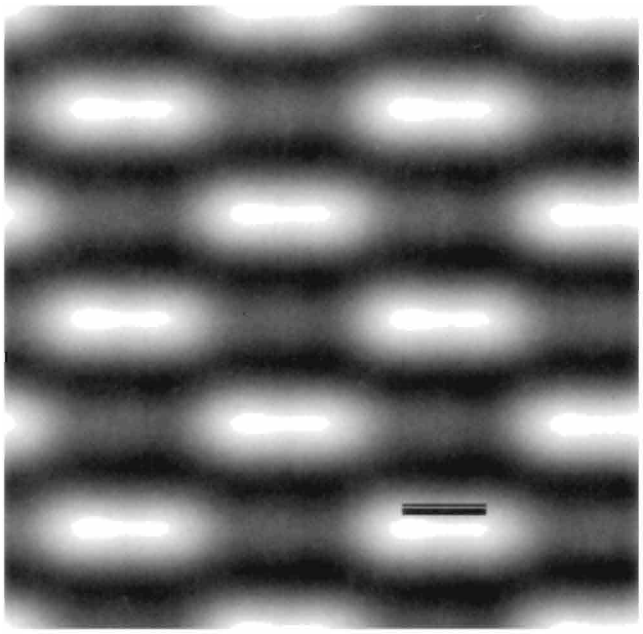

Figure 9. GaAs [110] HAADF simulated images for 1000-Å specimen, C_s 0.8 mm, accelerating voltage 100 kV, objective aperture 13.7 mrad. Bar: 1.41 Å.

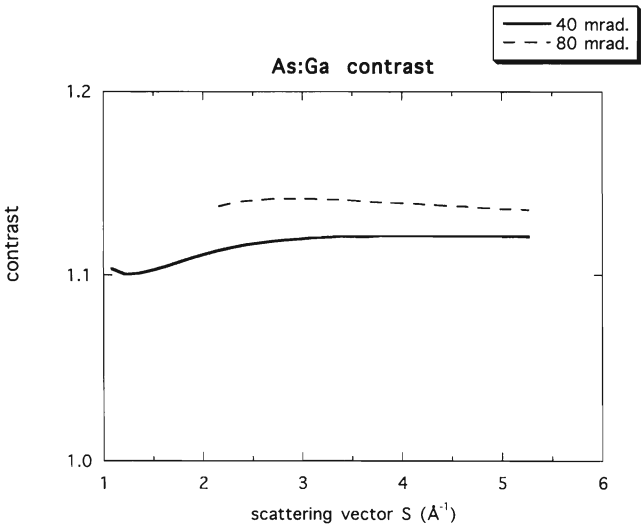

Figure 10. Ratio of As-to-Ga intensity as a function of detector outer cut-off wave vector for 40 mrad and 80 mrad inner detector angle.

distinguish columns of different atoms. We therefore calculated the images of 1000 Å of GaAs in the [110] projection shown in Figure 9. The dumbbells are made up from a Ga and an As column, which are indistinguishable in the image. Line profile plots show a small contrast. If the signal in the HAADF detector followed Rutherford scattering, then the contrast would be in the ratio of Z^2. In Figure 10 the As/Ga contrast is plotted for a 40 mrad and an 80 mrad inner cutoff as a function of outer detector angle. The signal does not vary much with the outer angle and the detector with an 80 mrad angle gives an As/Ga ratio of 1.19, which is close to the ratio of 1.13 expected for pure Rutherford scattering.

Another compound semiconductor that has been investigated by HAADF imaging is InP in the [100] projection. Calculations for a 100 kV microscope with an objective lens C_s of 0.8 mm and an objective aperture of 13 mrads semi-angle are shown as Figure 11 for a number of different thicknesses. In this projection the In and P atoms columns alternate. The contrast at the P column appears to strongly depend on defocus. This is more clearly demonstrated in the line traces along the [110] direction, which are shown as Figure 12. Examining probe profiles as a function of defocus shows that a subsidiary maximum can build up intensity between the atomic columns. Care should therefore be taken in directly interpreting the atomic column intensity as proportional to the square of atomic number in these circumstances.

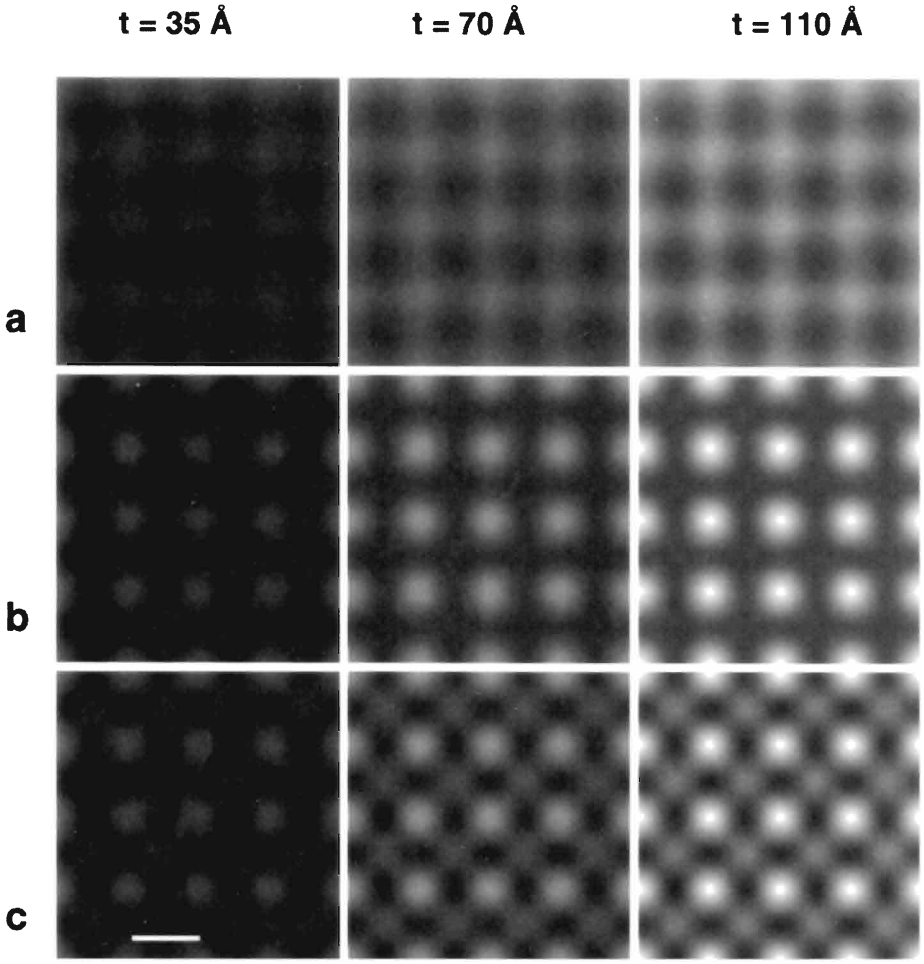

Figure 11. InP [100] HAADF simulated images for (**a**) 400 Å, (**b**) 600 Å, and (**c**) 800 Å defocus C_s 0.8 mm, accelerating voltage 100 kV, objective aperture 13 mrad. Bar: 3.24 Å.

Conclusions

Scattering by any mechanism to a HAADF can always be treated as a first-order perturbation. In crystalline specimens the dominant scattering mechanism is multiphonon excitation, often called thermal diffuse scattering. In the limit of high-angle scattering, this is identical to Rutherford scattering from a disordered array of atoms. Single-phonon scattering does not give the same limiting form of the cross section and single-phonon calculations could give spurious image features. Elastic scattering to the high-order Laue zone ring can be shown to contribute less than 10% to the signal in a HAADF detector, in agreement with experimental observation. Furthermore, elastic scattering to the HOLZ ring is highly concentrated in reciprocal space, and multislice calculations that do not sample reciprocal space with adequate precision might give misleading estimates of the proportion of elastically scattered electrons collected by the HAADF detector. Inelastic scattering from large energy loss

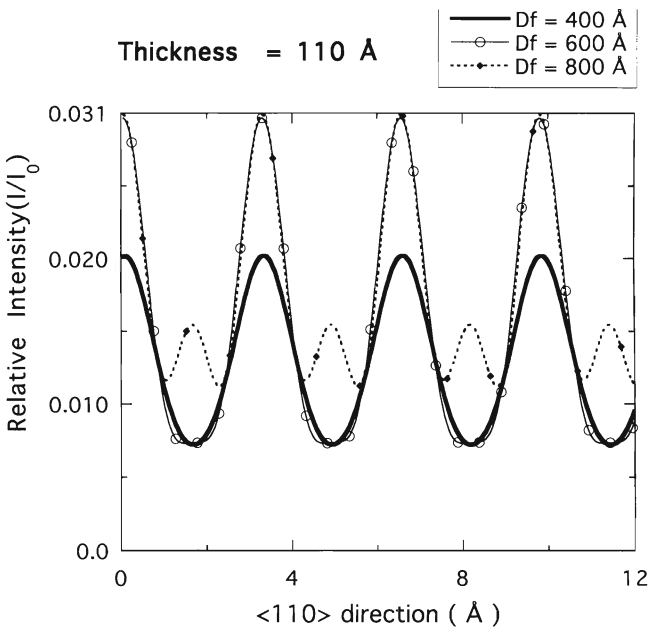

Figure 12. Line profiles along the [110] direction from the simulated images of the 110-Å InP specimen shown in Figure 11.

valence or inner shell excitations could also make a significant contribution to the HAADF signal for light elements.

The lattice resolution in HAADF images arises because they are formed with a coherent probe that subtends an angle greater than the Bragg angle for the lattice planes in the image. This is in accordance with the views of Spence and Cowley (1978). The contrast is due to the multiphonon thermal diffuse scattering which gives an approximate Z^2 dependence. The contrast mechanism can therefore be described as incoherent. The theory shows that it is not necessary for there to be dynamical elastic scattering before the thermal diffuse scattering to achieve localization on strings of atoms and hence, atomic resolution. In fact, experimental images of dislocations show that there must be more than one Bloch wave present and that the probe does not select only a single *s* state (Cowley and Huang, 1991). It has also been shown that dynamical elastic diffraction for electrons scattered into the HAADF detector has no effect, as it only redistributes intensity in the detector.

The theory provides an efficient way to calculate HAADF image contrast. Another advantage of the theory is that it should be possible to simulate defect contrast by substituting the appropriate dynamical diffraction propagator matrix $P_{gh}(\mathbf{q},z)$. Calculations for semiconductors in the [110] and [001] projections show that the contrast is relatively insensitive to thickness. The resolution, as expected, is related to the size of the coherently filled objective aperture. There are cases when the tails of the probe function could give spurious image intensities that might lead to errors in measurement of apparent Z for a column. It is also unfortunate that the multiphonon scattering can only be approximately described by an incoherent imaging model which assumes a simple local potential, analogous to an absorption potential. For quantitative analysis of HAADF images, it is necessary to calculate intensities using equations 38 or 39.

Imaging at high resolution using the HAADF signal is a promising method for detecting substitutions by one or two atoms in a single atomic column. The quantitative lattice imaging method of Ourmazd et al. (1990) also has this capability. It would therefore be interesting to compare the two methods in terms of their sensitivity at a given specimen dose.

Acknowledgments

We thank J.M. Cowley, J.C.H. Spence, J.M. Zuo, D. Jesson, and H. Rose for useful discussions. The use of computer equipment in the National Center for High Resolution Electron Microscopy supported by the National Science Foundation under grant DMR 911-5680 is also acknowledged.

References

Begbie GH (1947) Thermal scattering of X-rays by crystals II. The thermal scattering of the face-centered cubic and the close-packed hexagonal lattices. *Proc R Soc Lond* A188:189–207

Begbie GH, Born M (1947) Thermal scattering of X-rays by crystals I. Dynamical foundation. *Proc R SOC Lond A* 188:179–188

Buxton BF (1976) Bloch waves and higher order Laue zone effects in high energy electron diffraction. *Proc R SOC Lond A* 350:335–361

Buxton BF, Loveluck JE, Steeds JW (1978) Bloch waves and their corresponding atomic and molecular orbitals in high energy electron diffraction. *Philosophical Magazine A* 38:259–278

Cowley JM (1973a) High-resolution dark-field electron microscopy. I. Useful approximations. *Acta Crystallogr A* 29:529–536

Cowley JM (1973b) High-resolution dark-field electron microscopy. II. Short-range order in crystals. *Acta Crystallogr A* 29:537–541

Cowley JM, Huang Y (1992) De-channelling contrast in annular dark field STEM. *Ultramicroscopy* 40:171–180

Crewe AV, Wall J (1970) A scanning microscope with 5Å resolution. *J Mol Biol* 48:375–393

Crewe AV, Wall J, Welter LM (1968) A high resolution scanning transmission electron microscope. *J Appl Phys* 39:5861–5868

Doyle PA, Turner PS (1968) Relativistic Hartree-Fock X-ray and electron scattering factors. *Acta Crystallogr A* 24:390–397

Dudarev SL, Ryazanov MI (1988) Multiple scattering theory for fast electrons in single crystals and Kikuchi patterns. *Acta Crystallogr A* 44:51–61

Dudarev SL, Peng LM, Whelan MJ (1993) Correlations in space and time and dynamical diffraction of high energy electrons by crystals. *Phys Rev* B48:13408–13429

Earney JH (1971) Phonon scattering of fast electrons by crystals. *Phil Mag* 23:577–583

Egerton RF (1986) *Electron Energy Loss Spectroscopy in the Electron Microscope.* New York: Plenum Press.

Glauber RJ (1955) Time-dependent displacement correlations and inelastic scattering by crystals. *Phys Rev* 98:1692–1698

Goodman P, Moodie AF (1974) Numerical evaluation of N-beam

wave functions in electron scattering by the multi-slice method. *Acta Crystallogr A* 30:280–290

Hall CR, Hirsch PB (1965) Effect of thermal diffuse scattering on propagation of high energy electrons through crystals. *Proc R Soc Lond A* 286:158–177

Hillyard S, Silcox J (1993) Thickness effects in ADF STEM zone axis images. *Ultramicroscopy* 52:325–334

Hillyard S, Loane RF, Silcox J (1993) Annular dark-field imaging: Resolution and thickness effects. *Ultramicroscopy* 49:14–25

Hirsch PB, Howie A, Whelan MJ, Nicholson RB, Pashley DW (1965) *Electron Microscopy of Thin Crystals.* London: Butterworths.

Howie A (1979) Image contrast and localised signal selection techniques. *J Microsc* 17:11–23

Jesson DE, Pennycook SJ (1993) Incoherent imaging of thin specimens using coherently scattered electrons. *Proc Roy Soc Lond A* 441:261–281

Jesson DE, Pennycook SJ (1995) Incoherent imaging of crystals using thermally scattered electrons. *Proc Roy Soc Lond A* 449:273–393

Kirkland EJ, Loane RF, Silcox J (1987) Simulation of annular dark field STEM images using a modified multislice method. *Ultramicroscopy* 23:77–96

Kittle C (1986) *Introduction to Solid State Physicis.* New York: Wiley.

Konnert J, D'Antonio P (1991) Utilization of STEM nanodiffraction data. *Ultramicroscopy* 38:169–179

Loane RF, Kirkland EJ, Silcox J (1988) Visibility of single heavy atoms on thin crystalline silicon in simulated annular dark-field STEM images. *Acta Crystallogr A* 44:912–927

Loane RF, Xu P, Silcox J (1991) Thermal vibrations in convergent beam electron diffraction. *Acta Crystallogr A* 47:267–278

Loane RF, Xu P, Silcox J (1992) Incoherent imaging of zone axis crystals with ADF STEM. *Ultramicroscopy* 40:121–138

Ourmazd A, Baumann FH, Bode M, Kim Y (1990) Quantitative chemical lattice imaging: Theory and practice. *Ultramicroscopy* 34:237–255

Pennycook SJ, Boatner LA (1988) Chemically sensitive structure-imaging with a scanning transmission electron microscope. *Nature* 336:565–567

Pennycook SJ, Jesson DE (1990) High-resolution incoherent imaging of crystals. *Phys Rev Lett* 64:938–941

Pennycook SJ, Jesson DE (1991) High resolution Z-contrast imaging of crystals. *Ultramicroscopy* 37:14–38

Pennycook SJ, Berger SD, Culbertson RJ (1986) Elemental mapping with elastically scattered electrons. *J Microsc* 144:229–249

Perovic DD, Howie A, Rossouw CJ (1993) On the image contrast from dislocations in high-angle annular dark-field scanning transmission electron microscopy. *Phil Mag Lett* 67:261–272

Radi G (1970) Complex lattice potentials in electron diffraction calculated for a number of crystals. *Acta Crystallogr A* 26:41–56

Rez P (1977) Multiple inelastic scattering and dynamical diffraction. In: *50 Years of Electron Diffraction,* Dobson PJ, Humphreys CJ, Pendry JB (eds). London: Institute of Physics, pp 61–67

Rez P, Humphreys CJ, Whelan MJ (1977) The distribution of intensity in electron diffraction patterns due to phonon scattering. *Phil Mag* 35:81–96

Silcox J, Xu P, Loane RF (1992) Resolution limits in annular dark field STEM. *Ultramicroscopy* 47:173–186

Spence JCH, Cowley JM (1978) Lattice imaging in STEM. *Optik* 50:129–142

Spence JCH, Zuo JM, Lynch J (1989) On the HOLZ contribution to STEM lattice images formed using high-angle dark-field detectors. *Ultramicroscopy* 31:233–240

Treacy MMJ, Gibson JM (1993) Coherence and multiple scattering in "Z contrast" images. *Ultramicroscopy* 52:31–53

Treacy MMJ, Rice SB (1989) Catalyst particle sizes from Rutherford scattered intensities. *J Microsc* 156:211–234

Wang ZL, Cowley JM (1989a) Dynamic theory of high angle annular-dark field stem lattice images for a Ge/Si interface. *Ultramicroscopy* 32:275–289

Wang ZL, Cowley JM (1989b) Simulating high-angle annular dark-field STEM images including inelastic thermal diffuse scattering. *Ultramicroscopy* 31:437–454

Wright AG, Bird DM (1992) A density-matrix approach to coherence in high-energy electron diffraction. *Acta Crystallogr A* 47:215–221

Appendix A

In this appendix, the matrix element products for multiphonon (thermal diffuse) scattering used in the Imaging with Electrons Scattered to High Angles section, and the cross sections used in the High Angle Scattering section, are derived following the theory of Hall and Hirsch (Hall and Hirsch, 1965). For simplicity, we show the derivation for a unit cell with only one type of atom.

We start by assuming that the wave function for the

elastically scattered electrons at a depth z in a crystal can be expanded as a set of plane waves

$$\Phi(\mathbf{r}) = \sum_g \phi_g(z)\exp(i\mathbf{g}\cdot\mathbf{r}) \tag{A1}$$

where $\mathbf{g}$ is a reciprocal lattice vector. The amplitude of single scattering into a direction defined by $\mathbf{s}$ is then

$$\phi_s(\mathbf{s}) = \sum_g \sum_i \phi_g(z) f_{el}(s-g)\exp(i(\mathbf{s}-\mathbf{g})\cdot\mathbf{r}'_i) \tag{A2}$$

where $\mathbf{r}'_i$ are the instantaneous atomic positions and $f_{el}(\mathbf{s})$ are electron scattering fcctors. The intensity scattered to $\mathbf{s}$ is then

$$\begin{aligned} I_s(\mathbf{s}) = &\sum_g \sum_i \sum_j \phi_g^2(z) f_{el}^2(s-\mathbf{g})\exp(i(\mathbf{s}-\mathbf{g})\cdot(\mathbf{r}'_i - \mathbf{r}'_j)) \\ &+ \sum_g \sum_{h\neq g} \sum_i \sum_j \phi_g(z)\phi_h(z) f_{el}(s-g) f_{el}(s-h) \\ &\exp(i\mathbf{s}\cdot(\mathbf{r}'_i - \mathbf{r}'_j) - i\mathbf{g}\cdot\mathbf{r}'_i + \mathbf{ih}\cdot\mathbf{r}'_j) \end{aligned} \tag{A3}$$

The instantaneous position $\mathbf{r}'_i$ can be written as the sum of the static atom position $\mathbf{r}_i$ and a displacement $\mathbf{u}_i$ which could arise from thermal excitation. Explicitly separating terms referring to different atom positions gives

$$\begin{aligned} I_s(\mathbf{s}) = &\sum_g \phi_g^2(z) f_{el}^2(s-g)\Big[N + \\ &\sum_i \sum_{j\neq i} \exp(i(\mathbf{s}-\mathbf{g})\cdot(\mathbf{r}_i - \mathbf{r}_j))\,\overline{\exp(i(\mathbf{s}-\mathbf{g})\cdot(\mathbf{u}_i - \mathbf{u}_j))}\Big] \\ &+ \sum_g \sum_{h\neq g} \phi_g(z)\phi_h(z) f_{el}(s-g) f_{el}(s-h) \\ &\Big[\sum_i \exp(-i(\mathbf{g}-\mathbf{h})\cdot\mathbf{r}_i)\,\overline{\exp(-i(\mathbf{g}-\mathbf{h})\cdot\mathbf{u}_i)} \\ &+ \sum_i \sum_{j\neq i} \exp(i(\mathbf{s}-\mathbf{g})\cdot\mathbf{r}_i + i(\mathbf{s}-\mathbf{h})\cdot\mathbf{r}_j) \\ &\overline{\exp(-i(\mathbf{s}-\mathbf{g})\cdot\mathbf{u}_i + i(\mathbf{s}-\mathbf{h})\cdot\mathbf{u}_j)}\Big] \end{aligned} \tag{A4}$$

where the bar denotes time averaging and N is the number of atoms in the crystal. Time averaging gives the following relation for independently vibrating atoms

$$\overline{\exp[is\cdot(\mathbf{u}_i - \mathbf{u}_j)]} = \exp\left(-\frac{1}{2}s^2\overline{u^2}\right) = \exp(-Ms^2) \tag{A5}$$

where $\overline{u}^2$ is the mean square atomic displacement and M is the Debye Waller factor. Using equation A5 in equation A4 gives

$$\begin{aligned} I_s(\mathbf{s}) = &\sum_g \phi_g^2(z) f_{el}^2(s-g)\Big[N + \\ &\sum_i \sum_{j\neq i} \exp(i(\mathbf{s}-\mathbf{g})\cdot(\mathbf{r}_i - \mathbf{r}_j))\exp(-M(\mathbf{s}-\mathbf{g})^2)\Big] \\ &+ \sum_g \sum_{h\neq g} \phi_g(z)\phi_h(z) f_{el}(s-g) f_{el}(s-h) \\ &\Big[\sum_i \exp(-i(\mathbf{g}-\mathbf{h})\cdot\mathbf{r}_i)\exp(-M(\mathbf{g}-\mathbf{h})^2) \\ &+ \sum_i \sum_{i\neq i} \exp(i(\mathbf{s}-\mathbf{g})\cdot\mathbf{r}_i + i(\mathbf{s}-\mathbf{h})\cdot\mathbf{r}_j) \\ &\exp(-M(\mathbf{s}-\mathbf{g})^2)\exp(-M(\mathbf{s}-\mathbf{h})^2)\Big] \end{aligned} \tag{A6}$$

To determine the thermal diffuse contribution, the elastic scattering, $I_B(s)$, from the static atom positions $\mathbf{r}_i$ must be subtracted.

$$\begin{aligned} I_B(\mathbf{s}) = &\sum_g \phi_g^2(z) f_{el}^2(s-g)\exp(-M(\mathbf{s}-\mathbf{g})^2) \\ &\Big[N + \sum_i \sum_{j\neq i} \exp(i(\mathbf{s}-\mathbf{g})\cdot(\mathbf{r}_i - \mathbf{r}_j))\Big] \\ &+ \sum_g \sum_{h\neq g} \phi_g(z)\phi_h(z) f_{el}(s-g) f_{el}(s-h) \\ &\exp(-M(\mathbf{s}-\mathbf{g})^2)\exp(-M(\mathbf{s}-\mathbf{h})^2) \\ &\times \Big[\sum_i \exp(-i(\mathbf{g}-\mathbf{h})\cdot\mathbf{r}_i) \\ &+ \sum_i \sum_{j\neq i} \exp(i(\mathbf{s}-\mathbf{g})\cdot\mathbf{r}_i + i(\mathbf{s}-\mathbf{h})\cdot\mathbf{r}_j)\Big] \end{aligned} \tag{A7}$$

The final expression for the thermal diffuse intensity

$$\begin{aligned} I_{\mathrm{TDS}}(\mathbf{s}) = &\sum_g \phi_g^2(z) f_{el}^2(s-g)[1 - \exp(-M(\mathbf{s}-\mathbf{g})^2)]N \\ &+ \sum_g \sum_{h\neq g} \phi_g(z)\phi_h(z) f_{el}(s-g) f_{el}(s-h) N_{\mathrm{cell}} \\ &\sum_i \exp(-i(\mathbf{g}-\mathbf{h})\cdot\mathbf{r}_i) \times \\ &[\exp(-M(\mathbf{g}-\mathbf{h})^2) - \exp(-M(\mathbf{s}-\mathbf{g})^2) \\ &\exp(-M(\mathbf{s}-\mathbf{h})^2)] \end{aligned} \tag{A8}$$

where N_{cell} is the number of unit cells in the crystal and the summation over atomic positions is restricted to the unit cell. The first term can be identified with thermal diffuse or multiphonon scattering by a vector $\mathbf{s}-\mathbf{g}$ from a plane wave, while the second term results from the interference between two plane wave components identified by the reciprocal

lattice vectors **g** and **h.** To derive equation 18, which is a thermal diffuse scattering cross section per atom, the Mott formula equation 1, should be used for the electron scattering factor $f_{el}(s)$ and equation A8 divided by N.

$$dI_{\mathrm{TDS}}(\mathbf{s}) = \frac{4(Z - f_x(s))^2}{a_0^2 s^4}[1 - \exp(-Ms^2)]d\mathbf{s} \qquad \text{(A9)}$$

The second term is used in the expression for thermal diffuse scattering from convergent beam probes and is best expressed as an increase in scattered intensity per specimen depth per unit area. It appears in the Imaging with Electrons Scattered to High Angles section as a product of matrix elements. Again, the Mott formula for the electron scattering factor is substituted in A8 to give

$$\frac{dI_{\mathrm{TDS}}(\mathbf{s})}{dz} = H(\mathbf{s}-\mathbf{g})H^*(\mathbf{s}-\mathbf{h}) =$$

$$\frac{4}{a_0^2 V_c}\sum_i \exp(-i(\mathbf{g}-\mathbf{h})\cdot\mathbf{r}_i)\frac{[Z - f_x(s-g)][Z - f_x(s-h)]}{(\mathbf{s}-\mathbf{g})^2(\mathbf{s}-\mathbf{h})^2}$$
$$\times \{\exp[-M(\mathbf{g}-\mathbf{h})^2] - \exp[-M(\mathbf{s}-\mathbf{g})^2]\exp[-M(\mathbf{s}-\mathbf{h})^2]\} \qquad \text{(A10)}$$

which is similar to the expression for multiphonon scattering derived by Radi for anomalous absorption due to phonon scattering (Radi, 1970). This can be easily generalized to

$$H(\mathbf{s}-\mathbf{q}-\mathbf{g})H^*(\mathbf{s}-\mathbf{q}-\mathbf{h}) = \frac{4}{a_0^2 V_c}\sum_i \exp(-i(\mathbf{g}-\mathbf{h})\cdot\mathbf{r}_i)\frac{[Z_i - f_x^i(s-q-g)][Z_i - f_x^i(s-q-h)]}{(\mathbf{s}-\mathbf{q}-\mathbf{g})^2(\mathbf{s}-\mathbf{q}-\mathbf{h})^2}$$
$$\times \left\{\exp\left[-M_i(\mathbf{g}-\mathbf{h})^2\right] - \exp\left[-M_i(\mathbf{s}-\mathbf{q}-\mathbf{g})^2\right]\exp\left[-M_i(\mathbf{s}-\mathbf{q}-\mathbf{h})^2\right]\right\} \qquad \text{(A11)}$$

where Z_i is the atomic number, f_x^i is the X-ray scattering factor, and M_i is the Debye-Waller factor for atom of type i, when there is more than one type of atom in the unit cell.

To derive the equivalent expression for a general phonon dispersion, the Glauber correlation function should be used (Glauber, 1955). Equation A10 now becomes

$$\frac{dI_{\mathrm{TDS}}(s)}{dz} = H(\mathbf{s}-\mathbf{g})H^*(\mathbf{s}-\mathbf{h}) =$$

$$\frac{4}{a_0^2 V_c}\frac{[Z - f_x(\mathbf{s}-\mathbf{g})][Z - f_x(\mathbf{s}-\mathbf{h})]}{(\mathbf{s}-\mathbf{g})^2(\mathbf{s}-\mathbf{h})^2}\sum_i \exp(-i(\mathbf{g}-\mathbf{h})\cdot\mathbf{r}_i)$$
$$\times \sum_j \exp\left[i(s + \frac{(\mathbf{h}-\mathbf{g})}{2})\Delta\mathbf{R}_{ij}\right]\exp[-M(\mathbf{s}-\mathbf{g})^2]$$
$$\exp[-M(\mathbf{s}-\mathbf{h})^2]\{\exp[(\mathbf{s}-\mathbf{g})C(\Delta\mathbf{R}_{ij})(\mathbf{s}-\mathbf{h})] - 1\} \qquad \text{(A12)}$$

where $\Delta\mathbf{R}_{ij} = \mathbf{r}_i - \mathbf{r}_j$ is the atomic separation and $C(\Delta\mathbf{R}_{ij})$ is the correlation function which, for simple systems with one type of atom, is given by

$$C(\Delta\mathbf{R}_{ij}) = \frac{\hbar V_c}{(2\pi)^3 M_a}\sum_p \mathbf{e}^p\mathbf{e}^p\int\frac{dk}{\omega_p(k)}\left(\exp(i\mathbf{k}\cdot\Delta\mathbf{R}_{ij}) + \frac{2\cos(i\mathbf{k}\cdot\Delta\mathbf{R}_{ij})}{\exp(\beta\hbar\omega) - 1}\right) \qquad \text{(A13)}$$

where M_a is the atomic mass, β is $1/k_BT$, T is the temperature, and $\mathbf{e}_p$ refers to the phonon polarization. In the Einstein model $C(\Delta\mathbf{R}_{ij})$ is $\bar{u}^2\delta_{i,j}$ and A12 reduces to A10. If an isotropic Debye model is used for phonon dispersion then equation A12 can be approximately integrated, giving a sinc function in atomic separation (Jesson and Pennycook, 1995). Even under these circumstances, "coherence" is maintained only over about 3–7 interatomic spacings.

Appendix B

Contribution of Inelastic Scattering to the HAADF Detector

Although it is generally believed that inelastic scattering is strongly forward peaked and has little chance of reaching a high-angle detector, a small but significant fraction of inelastically scattered electrons can be scattered through large angles in the form of Compton scattering. The general expression for the differential scattering cross section for inelastic scattering is

$$\frac{d^2I}{dEd\Omega} = \frac{4n_i}{a_0^2}\frac{|\langle\psi_f^*|\exp(i\mathbf{q}\cdot\mathbf{r})|\psi_i\rangle|^2}{q^4} \qquad \text{(B1)}$$

where q is the scattering wave vector and ψ_i and ψ_f are the initial and final state wave functions, respectively, and n_i is the number of electrons in atomic subshell i. At high enough energies above an edge threshold, the electron in the final state is little influenced by the potential of the solid and can be expressed as a plane wave, wave vector $\mathbf{k}_f$.

$$\frac{d^2I}{dEd\Omega} = \frac{4n_i}{a_0^2} \frac{|\langle \exp(-i\mathbf{k}_f \cdot \mathbf{r})|\exp(i\mathbf{q} \cdot \mathbf{r})\psi_i\rangle|^2}{q^4} \quad \text{(B2)}$$

The initial state wave function ψ_i is slowly varying, compared with the rapid oscillations of the final state plane wave and, to a first approximation, can be assumed constant. Performing the integral for the matrix element gives $\delta(\mathbf{k}_f - \mathbf{q})$. When the energy transfer is large, the binding energy of the atomic electron is insignificant and the excited electron behaves as if it was a free electron with energy $E = \hbar^2 q^2/2m$. At an energy E above the threshold for that subshell, the spectrum only has electrons scattered by a wave vector $q = \sqrt{2mE}/\hbar$. This sharp feature is known as the Bethe ridge and gets narrower with increasing energy above threshold. The differential cross section becomes

$$\frac{d^2I}{dEd\Omega} = \frac{4n_i}{a_0^2} \frac{\delta\left(E - \frac{\hbar^2 q^2}{2m}\right)}{q^4} \quad \text{(B3)}$$

Only electrons with energy from $E_i = \hbar^2 q_i^2/2m$ to $E_f = \hbar^2 q_f^2/2m$ will contribute to the signal observed by the HAADF detector where q_i and q_f define the inner and outer cutoff wave vectors for the detector. Integrating the signal from E_i to E_f is equivalent to integrating the signal between q_i and q_f. The integral cross section becomes

$$\phi = \int_{q_i}^{q_f} \frac{4n_i}{a_0^2} \frac{1}{q^4} \frac{2\pi q dq}{K^2} = \frac{4\pi n_i}{K^2 a_0^2} \left(\frac{1}{q_f^2} - \frac{1}{q_i^2}\right) \quad \text{(B4)}$$

where K is the fast electron wave vector.

This can be compared to an approximate value for the integrated Rutherford scattering with the same limits.

$$\phi_{el} = \int_{q_i}^{q_f} \frac{4Z^2}{a_0^2} \frac{1}{q^4} \frac{2\pi q dq}{K^2} = \frac{4\pi Z^2}{K^2 a_0^2} \left(\frac{1}{q_f^2} - \frac{1}{q_i^2}\right) \quad \text{(B5)}$$

The sum over subshells is approximately given by the atomic number $Z = \sum_i n_i$, assuming that the contribution from subshells whose binding energy is a sizable fraction of the beam electron energy is relatively small. Comparing equations B4 and B5 shows that the ratio of elastic to inelastic scattering in the HAADF detector is Z, the atomic number. For first-row light elements some estimate of the inelastic contribution to the detector should be included if better than 10% accuracy is desired in the calculation.